INTERNATIONAL JOURNAL OF LATEST TECHNOLOGY IN ENGINEERING, MANAGEMENT & APPLIED SCIENCE (IJLTEMAS)

ISSN 2278-2540 | DOI: 10.51583/IJLTEMAS | Volume XV, Issue IX, September 2026

Mathematical Model for Dynamic Behavior of Elastic Euler-Bernoulli Beam under Moving-Induced Distributed Load

A. Adedowole

Department of Mathematical Sciences, Adekunle Ajasin University, Akungba-Akoko, Nigeria

DOI: https://doi.org/10.51583/IJLTEMAS.2026.150900160

Received: 07 October 2026; Accepted: 12 October 2026; Published: 26 October 2026

ABSTRACT

This work examines the transient deflection of a simply supported Euler–Bernoulli beam on a Winkler elastic foundation subjected to a finite-length distributed load moving at constant speed. The excitation has either a constant-amplitude or sinusoidally modulated form and includes a dimensionally specified power-law induced-load factor. To correct the ambiguity in an earlier moving-front representation, the applied loading is confined to a finite contact footprint with explicit entry and exit from the span. A Fourier-sine expansion reduces the governing fourth-order beam equation to modal oscillators, which are evaluated using Duhamel convolution and average-acceleration Newmark integration. Independent two-node cubic Hermite beam elements provide numerical verification. For a representative 50.192 m beam with a 3 m footprint, 12.5 m/s speed, and Winkler coefficient of 0.20 MN/m², the 32-mode constant-load solution gives a peak midspan deflection of 4.5964 mm, compared with 4.5964 mm from a 100-element finite-element model. Increasing the induced-rate parameter from 0 to 0.20 s^{-1} increases the calculated constant-load peak from 4.5964 to 6.6440 mm. Under the specified undamped harmonic forcing at the first supported-beam natural frequency, the peak reaches 54.2900 mm, although the outcome is strongly frequency dependent. Modal convergence, point-force limiting behaviour, finite-element agreement, frequency estimates, and foundation-stiffness and velocity sweeps support the consistency of the revised calculations. The results establish parameter-dependent amplification for the stated linear moving-force model, not a universal increase under harmonic excitation. Limitations concerning moving-mass inertia, damping, support variability, and experimental calibration are identified.

Keywords: elastic Foundation, Euler-Bernoulli beam, Moving Loads, Induced-Load Factor, Distributed Load Fourier sine transform**.**

1. INTRODUCTION

The vibration of beams subjected to travelling loads remains an important problem in structural mechanics because the response is governed by the motion of the excitation as well as by the properties of the structure. A load traversing a span changes the spatial distribution of the applied force continuously, thereby producing transient displacements and internal forces that cannot generally be inferred from a corresponding static loading condition. Frýba [1] developed a comprehensive theoretical treatment of structures under moving loads, while Ouyang [2] clarified the principal distinctions between moving-force, moving-mass, and related dynamic problems. Earlier work by Kenney [3] established the importance of foundation resistance in the vibration of beams under moving excitation. These fundamental contributions provided the basis for later investigations in which travelling speed, excitation duration, structural natural frequencies and support flexibility were examined together.

The significance of this interaction is particularly evident in transportation structures, where a sequence of moving loads may excite a beam repeatedly during a relatively short period. Museros et al. [4] derived conditions associated with resonance and cancellation of free vibrations in simply supported bridge beams, demonstrating that increased speed does not necessarily produce a monotonically increasing response. Yang et al. [5] likewise investigated beams traversed by high-speed trains and showed the influence of vehicle speed and loading sequence on the vibration characteristics. Moving-load analysis has subsequently been extended

ISSN 2278-2540 | DOI: 10.51583/IJLTEMAS | Volume XV, Issue IX, September 2026

beyond the isolated beam to the coupled transport system. Zhai et al. [6] reviewed train-track-bridge interaction, Lamprea-Pineda et al. [7] assessed the applications and limitations of beams on elastic foundations in railway engineering, and Sayeed and Shahin [8] studied track-ground interaction using three-dimensional finite-element modelling. Although such comprehensive models provide greater physical detail, simpler beam formulations remain valuable for isolating the effects of individual loading and foundation parameters and for establishing analytical benchmarks.

One of the principal requirements in a simplified structural model is an appropriate description of the supporting medium. Hetényi [9] presented the classical theory of beams resting on elastic foundations, in which the foundation supplies a restoring reaction related to transverse displacement. Saito and Terasawa [10] subsequently examined the steady-state response of a beam on a Pasternak-type foundation under travelling loads, thereby extending the representation of the support beyond independent springs. The influence of foundation variability was addressed by Dimitrovová [11], who analysed moving-load response across piecewise homogeneous support regions, and by Castro Jorge et al. [12], who investigated beams on non-uniform and nonlinear foundations and quantified the significance of stiffness, damping and critical velocity. These findings demonstrate that a foundation cannot be treated merely as a passive geometric constraint: its mechanical resistance modifies the frequencies and magnitudes of the moving-load response. For a uniform, slender beam, however, a Winkler foundation offers a tractable reference model in which the role of foundation stiffness can be examined explicitly.

The mathematical description of the travelling excitation is as important as the foundation model. Abu-Hilal and Zibdeh [13] obtained solutions for beams with several end conditions under moving forces travelling at constant or variable speeds, while Abu-Hilal and Mohsen [14] examined the additional influence of harmonic variation in the travelling force. The distinction between a prescribed moving force and a travelling mass was emphasised by Esmailzadeh and Ghorashi [15], who studied beams traversed by partially distributed moving masses. In the moving-mass problem, inertial interaction is coupled to the beam motion; in the prescribed-force problem, the time-varying load distribution acts externally. The present investigation adopts the latter description. Consequently, its results concern a force with specified intensity and contact region rather than a complete vehicle-structure interaction model, and this distinction is retained in the interpretation of the numerical results.

Beyond the moving-force/moving-mass distinction, the temporal character of the applied force is central to resonance. Wu and Gao [16] obtained analytical responses for a viscously damped double-beam system under moving harmonic loads, highlighting the combined effects of travelling velocity, excitation frequency and interconnecting-layer properties. Şimşek and Kocatürk [17] examined the vibration of functionally graded beams under concentrated moving harmonic excitation, while Şimşek and Al-Shujairi [18] investigated successive harmonic moving loads on sandwich beams. These studies demonstrate that harmonic modulation introduces a forcing frequency in addition to the frequencies created by translation over the beam span. They also show why the response to a harmonic load cannot be characterised by its peak force alone: frequency ratio, phase, load spacing and residence time can alter dynamic amplification. A meaningful comparison between constant and harmonic cases therefore requires the same structural properties, foundation conditions and explicitly defined reference load intensities.

More refined beam and foundation models have been developed to address behaviour not represented by the classical Euler–Bernoulli formulation. Calim [19] analysed axially functionally graded Timoshenko beams on viscoelastic foundations, and Li et al. [20] derived analytical results for functionally graded beams with varying cross-sections on Pasternak supports. Su et al. [21] investigated coupled beams on variable viscoelastic foundations, Ermis et al. [22] developed a mixed finite-element approach for axially graded curved beams, and Vu et al. [23] considered sandwich beams carrying moving masses with partial foundation support. These developments are relevant because they clarify the limitations of a uniform slender-beam approximation. Nevertheless, incorporating all such mechanisms simultaneously would obscure the separate effect of time-varying distributed load intensity. The present work therefore retains the linear Euler–Bernoulli assumptions of a uniform cross-section, small deflection and simply supported ends, while acknowledging

ISSN 2278-2540 | DOI: 10.51583/IJLTEMAS | Volume XV, Issue IX, September 2026

that shear deformation, rotary inertia, structural damping and more elaborate soil–structure interaction may become important outside the chosen parameter regime.

The relationship between the present formulation and earlier analytical research also requires clear identification. Adedowole [24] studied an Euler-Bernoulli beam on an elastic foundation under two concentrated moving loads, applying Fourier sine analysis to investigate the effects of load separation and other parameters. Omolofe and Adedowole [25] examined moving distributed masses in a beam problem involving time-dependent boundary conditions, while Omolofe and Adara [26] considered accelerating masses and axial loading under general support conditions. Together, these contributions established useful techniques for moving-load problems, but they involve loading or boundary configurations that are different from a finite-length prescribed distributed force whose amplitude evolves according to a specified power law. The distinction is important: changing the amplitude of a prescribed force is not equivalent to introducing moving-mass inertia, and an analysis of concentrated loads does not automatically describe the entry and exit of a distributed load footprint.

Recent investigations further indicate that both loading and support modelling remain active areas of research. Huang et al. [27] analysed non-uniform functionally graded beams on inhomogeneous foundations under moving distributed loads and demonstrated the usefulness of a spectral formulation for more complicated spatial coefficients. Chen and Lin [28] investigated bidirectionally graded beams under moving harmonic excitation and evaluated the effects of foundation parameters and excitation characteristics. These studies also show that Fourier-based expansions are only one of several possible analytical and numerical strategies. They provide strong reasons to avoid describing a time-dependent load factor, an elastic foundation, or a Fourier series in isolation as an entirely new concept. Rather, the contribution of a particular study must be identified in its clearly defined forcing function, boundary-value problem, derived response and evidence of computational correctness.

For a simply supported uniform Euler-Bernoulli beam, a Fourier sine expansion is particularly useful because its basis functions satisfy the zero-deflection and zero-bending-moment end conditions. Projection of the governing fourth-order partial differential equation onto this basis gives modal equations whose forcing terms can be obtained by integrating the actual moving-load footprint over the beam span. Analytical convolution can then be used to calculate the transient response of the retained modes. The choice is motivated by the transparency of the resulting modal frequencies and forcing terms, not by an assumption that Fourier analysis is universally more accurate than other methods. Independent numerical procedures remain necessary to assess errors from mode truncation and time integration. In this regard, Newmark [29] supplied a standard framework for structural time stepping, while Bathe [30] presented finite-element procedures suitable for independently checking displacement and internal-force predictions.

The specific issue addressed in the present study is the response of a simply supported, uniform Euler-Bernoulli beam on a Winkler foundation to a prescribed distributed moving load whose amplitude changes with time. The induced-load factor is defined through a dimensionally consistent power-law envelope multiplying a finite-length travelling-force distribution. Its role is to represent prescribed growth or decay of force intensity during passage; it does not represent vehicle mass accumulation, impact dynamics or a new constitutive law for the beam. Constant-amplitude and harmonically modulated cases are treated within the same framework, allowing the effects of amplitude variation and imposed oscillatory frequency to be distinguished. These features define a specific comparison, although previous studies have already considered time-dependent moving forces and distributed loads in other configurations.

Accordingly, the research gap lies in the need for a transparent and verifiable comparative treatment of this particular finite-footprint, power-law-modulated loading model, rather than in the general absence of moving-load solutions. The study develops the modal equations and their time-domain responses, establishes reductions to appropriate limiting cases, and evaluates how the induced-load parameter, foundation stiffness, travelling speed and harmonic frequency affect transverse displacement, bending moment and shear force. Natural frequencies, estimated resonance conditions and modal convergence are reported, and the Fourier-modal solution is compared with an independent finite-element computation. Through these analyses, the

ISSN 2278-2540 | DOI: 10.51583/IJLTEMAS | Volume XV, Issue IX, September 2026

study aims to distinguish the physical consequences of the prescribed loading history from artefacts of load representation or numerical truncation, while clearly stating the limitations of the linear beam–foundation idealization.

2. METHODOLOGY

2.1. Formulation of the beam–foundation problem

A uniform, straight, slender Euler–Bernoulli beam of length L is considered on a continuous, linearly elastic Winkler foundation (Figure 1). The beam possesses Young's modulus E, second moment of area I, cross-sectional area A, material density ρ, and mass per unit length $\mu = \rho A$. The distributed excitation travels from $x = 0$ towards $x = L$ at a prescribed constant speed v. The transverse deflection $w(x,t)$ is positive in the direction of the applied load. The beam is initially at rest, and its ends are simply supported. A uniform tensile axial force $N \geq 0$ is retained in the general equation; $N = 0$ describes the unprestressed baseline. Only prescribed moving-force loading is considered: acceleration of a travelling mass relative to the vibrating beam is excluded.

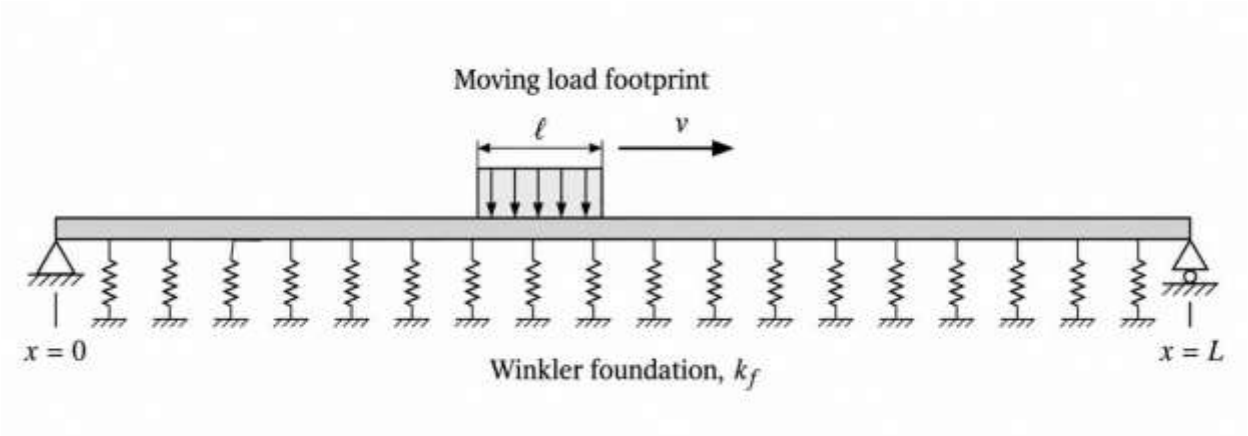


Figure 1. Physical configuration of the simply supported Euler–Bernoulli beam resting on a Winkler foundation and subjected to a finite-length distributed moving force.

The governing transverse equilibrium equation is

$$EI\, w_{xxxx}(x,t) - N w_{xx}(x,t) + \mu w_{tt}(x,t) + k_f w(x,t) = q(x,t), \quad 0 < x < L. \tag{1}$$

The foundation coefficient k_f represents the restoring force **per unit beam length per unit displacement** (N/m²); it must not be confused with an area-based subgrade modulus (N/m³), whose conversion for a beam of width b requires the appropriate effective support width. Tensile N contributes positively to lateral stiffness in the adopted sign convention. The model excludes transverse shear deformation, rotary inertia, foundation damping and separation from the support. These restrictions are appropriate to a first-order benchmark for slender beams, not a fully calibrated vehicle–bridge or soil–structure model.

2.2. Boundary and initial conditions

For an Euler–Bernoulli beam the bending moment is proportional to w_{xx}. Simple supports impose zero transverse displacement and zero end bending moment:

$$w(0,t) = w(L,t) = 0, \tag{2}$$

$$EIw_{xx}(0,t) = EIw_{xx}(L,t) = 0. \tag{3}$$

The initial conditions are displacement and **velocity**, not displacement and acceleration:

ISSN 2278-2540 | DOI: 10.51583/IJLTEMAS | Volume XV, Issue IX, September 2026

$$w(x,0) = 0, \qquad w_t(x,0) = 0. \tag{4}$$

These conditions permit the sine eigenfunctions used below. The expression $w_{xx} = 0$ must not be replaced by $w_x = 0$, which would impose a slope restriction incompatible with a simply supported beam.

2.3. Finite-footprint moving force and induced-load parameter

Let the travelling load have physical contact length ℓ and leading edge $\xi(t) = vt$, so its unloaded-to-loaded transition extends from $vt - \ell$ to vt. With $H(z)$ the Heaviside function, its footprint indicator is defined by

$$\chi(x,t) = H(x - vt + \ell) - H(x - vt). \tag{5}$$

This difference, unlike a single $H(x - vt)$, selects **only a finite moving interval**. The actual contact region is the intersection of the footprint with the beam, whose endpoints are

$$c(t) = \max\{0, vt - \ell\}, \qquad b(t) = \min\{L, vt\}. \tag{6}$$

The applied load is zero whenever $b(t) \le c(t)$. The prescribed load intensity varies through a dimensionless power-law envelope

$$p(t) = p_0(1 + at)^r, \qquad p_0 > 0, \quad 1 + at > 0, \tag{7}$$

where p_0 is the reference force per unit length (N/m), a is the induced-load rate (s^{-1}), and r is a dimensionless exponent. Thus, a parameter called an *induced-load factor* in the earlier manuscript is specified here without ambiguity. A positive a increases the imposed intensity for $r > 0$, whereas a negative a (while $1 + at > 0$) reduces it. This is a **prescribed force-envelope model**, not a derivation of changing vehicle mass from a conservation law. For $r = 1$ it becomes $p(t) = p_0(1 + at)$, permitting elementary antiderivatives on each contact interval.

The two loading cases analysed are

$$q_C(x,t) = p_0(1 + at)^r \chi(x,t), \tag{8}$$

$$q_H(x,t) = p_0(1 + at)^r \sin(\Omega t)\chi(x,t). \tag{9}$$

Here Ω is the imposed angular frequency (rad/s). The subscripts C and H distinguish a non-oscillatory intensity history from its harmonic counterpart. When $a = 0$, q_C is a **constant-intensity** moving load; when $a \neq 0$, q_C is non-oscillatory but not constant in amplitude. The signed harmonic factor $\sin(\Omega t)$ represents an oscillatory external-force component and can become negative. If a strictly non-negative wheel force is intended, an offset factor such as $1 + \eta\sin(\Omega t)$ must be specified and calculated separately.

While the full footprint is on the beam, the force resultant is $P(t) = p_0\ell(1 + at)^r$ for Case C, and $P(t)\sin(\Omega t)$ for Case H. During entry and exit the contact length reduces to $b(t) - c(t)$. The single-load passage finishes at $t_{\text{exit}} = (L + \ell)/v$.

2.4. Fourier sine transformation and modal reduction

The finite-span Fourier sine functions naturally satisfy both simply supported conditions. Introduce the wavenumbers $\kappa_n = n\pi/L$ and approximate the deflection by

$$w(x,t) = \sum_{n=1}^{N_m} y_n(t)\sin(\kappa_n x), \qquad \kappa_n = \frac{n\pi}{L}. \tag{10}$$

Differentiation gives $w_{xxxx} = \sum_n \kappa_n^4 y_n \sin(\kappa_n x)$, $w_{xx} = -\sum_n \kappa_n^2 y_n \sin(\kappa_n x)$, and $w_{tt} = \sum_n \ddot{y}_n \sin(\kappa_n x)$. After substituting into the governing equation, multiplying by $\sin(\kappa_m x)$ and integrating from 0 to L, the orthogonality identity is applied:

ISSN 2278-2540 | DOI: 10.51583/IJLTEMAS | Volume XV, Issue IX, September 2026

$$\int_0^L \sin(\kappa_m x)\sin(\kappa_n x)\,dx = \frac{L}{2}\delta_{mn}. \tag{11}$$

Consequently, the beam is reduced to independent modal oscillators:

$$\ddot{y}_n(t) + \omega_n^2 y_n(t) = \frac{F_n(t)}{\mu}, \tag{12}$$

$$\omega_n = \sqrt{\frac{EI\kappa_n^4 + N\kappa_n^2 + k_f}{\mu}}, \qquad F_n(t) = \frac{2}{L}\int_0^L q\,(x,t)\sin(\kappa_n x)\,dx. \tag{13}$$

Here ω_n is the natural circular frequency of the undamped supported beam (rad/s), and $F_n(t)$ is the generalised forcing intensity (N/m). Frequencies in cycles per second are $f_n = \omega_n/(2\pi)$. The corresponding normalised mode shapes are $\phi_n(x) = \sin(n\pi x/L)$; these are unchanged by uniform Winkler stiffness and uniform tensile prestress in the present idealization, whereas their frequencies change.

2.4.1. Exact projection of a partially supported moving footprint

Projecting the finite distributed force over its actual contact interval yields

$$F_n(t) = \frac{2p_0(1+at)^r s(t)}{L}\int_{c(t)}^{b(t)} \sin(\kappa_n x)\,dx, \tag{14}$$

where $s(t) = 1$ in Case C and $s(t) = \sin(\Omega t)$ in Case H. Integration gives

$$F_n(t) = \frac{2p_0(1+at)^r s(t)}{L\kappa_n}\left[\cos\big(\kappa_n c(t)\big) - \cos\big(\kappa_n b(t)\big)\right], \quad b(t) > c(t), \tag{15}$$

and $F_n(t) = 0$ outside the contact interval. This expression is dimensionally consistent and accounts for the complete entrance–traversal–exit history.

For $0 < l < L$ and $v > 0$, the geometric factor in square brackets can be evaluated piecewise:

$$B_n(t) = \begin{cases} 1 - \cos(\kappa_n v t), & 0 < t < l/v, \\ \cos\big(\kappa_n(vt - \ell)\big) - \cos(\kappa_n v t), & \ell/v \le t \le L/v, \\ \cos\big(\kappa_n(vt - \ell)\big) - (-1)^n, & L/v < t < (L+\ell)/v, \\ 0, & \text{otherwise.} \end{cases} \tag{16}$$

Thus $F_n(t) = [2p_0(1+at)^r s(t)/(L\kappa_n)]B_n(t)$ with no artificial extension of the load outside the beam. A beam subjected to several footprints can be handled by superposing one such force term for each footprint and its specified edge trajectory.

2.5. Laplace transformation and exact modal convolution

The transformed modal equation, with the zero initial conditions, reads

$$(s^2 + \omega_n^2)Y_n(s) = \frac{\hat{F}_n(s)}{\mu}, \tag{17}$$

where $Y_n(s) = \mathscr{L}\{y_n(t)\}$ and $\hat{F}_n(s) = \mathscr{L}\{F_n(t)\}$. Hence,

$$Y_n(s) = \frac{\hat{F}_n(s)}{\mu(s^2+\omega_n^2)}. \tag{18}$$

The inverse transform gives the causal impulse response $g_n(t) = \sin(\omega_n t)/(\mu\omega_n)$. Application of the convolution theorem produces

ISSN 2278-2540 | DOI: 10.51583/IJLTEMAS | Volume XV, Issue IX, September 2026

$$y_n(t) = \frac{1}{\mu\omega_n}\int_0^t F_n(\tau)\sin[\omega_n(t-\tau)]d\tau. \quad (19)$$

The full displacement field is therefore

$$w(x,t) = \sum_{n=1}^{N_m}\frac{\sin(\kappa_n x)}{\mu\omega_n}\int_0^t F_n(\tau)\sin[\omega_n(t-\tau)]d\tau. \quad (20)$$

The temporal convolution is exact for each retained oscillator when its prescribed forcing is integrated exactly. The full beam response remains a **spatial approximation** for finite N_m. The forcing $F_n(t)$ is evaluated with the piecewise footprint limits; omitting these limits would invalidate a claimed whole-passage closed-form solution.

2.5.1. Constant-intensity and linear induced-load limits

To show the analytical reduction explicitly, first let $a = 0$ and consider the stage in which the entire footprint lies on the beam. Trigonometric rearrangement of the projected force gives

$$F_n(t) = C_n\sin(\lambda_n t - \varphi_n), \quad C_n = \frac{4p_0}{L\kappa_n}\sin\left(\frac{\kappa_n \ell}{2}\right), \quad \lambda_n = \kappa_n v, \quad \varphi_n = \frac{\kappa_n \ell}{2}. \quad (21)$$

For a forcing component applied from a zero-state segment origin, introduce the standard response kernels

$$\mathcal{S}(\omega,\lambda,t) = \frac{\sin(\lambda t)-(\lambda/\omega)\sin(\omega t)}{\omega^2-\lambda^2}, \quad (22)$$

$$\mathcal{C}(\omega,\lambda,t) = \frac{\cos(\lambda t)-\cos(\omega t)}{\omega^2-\lambda^2}. \quad (23)$$

The corresponding zero-state forced contribution is

$$y_n^{(0)}(t) = \frac{C_n}{\mu}[\cos\varphi_n\,\mathcal{S}(\omega_n,\lambda_n,t) - \sin\varphi_n\,\mathcal{C}(\omega_n,\lambda_n,t)]. \quad (24)$$

This is a **building block for an individual full-footprint segment**, not a whole-passage solution: the displacement and velocity inherited from the preceding entry interval must be added through the homogeneous solution. The complete convolution given above automatically enforces continuity at all entry and exit events. When $r = 1$, the multiplier $(1 + at)$ adds terms involving the first time moment of each trigonometric forcing component; these are obtained by direct integration, without introducing undefined coefficients such as Ψ, h_0, or z_k from the earlier draft.

2.5.2. Harmonic modulation and forcing sidebands

For $a = 0$ on the full-footprint segment, multiplication of the spatially projected force by $\sin(\Omega t)$ gives

$$F_n^H(t) = \frac{C_n}{2}[\cos((\lambda_n-\Omega)t-\varphi_n) - \cos((\lambda_n+\Omega)t-\varphi_n)]. \quad (25)$$

Thus harmonic modulation generates sideband frequencies $|\lambda_n - \Omega|$ and $\lambda_n + \Omega$. For $a \neq 0$ these terms acquire the common power-law envelope $(1 + at)^r$, which changes their finite-duration amplitudes and broadens their transient spectral content. It does **not** alter the natural frequencies ω_n, since the beam mass and stiffness matrices have not changed.

2.6. Analytical verification through limiting cases

Three reduction tests follow directly from the derived equations. First, eliminating the elastic foundation sets $k_f = 0$ and reduces the modal frequency to

ISSN 2278-2540 | DOI: 10.51583/IJLTEMAS | Volume XV, Issue IX, September 2026

$$\omega_n^{(0)} = \sqrt{\frac{EI\kappa_n^4 + N\kappa_n^2}{\mu}}. \tag{26}$$

Second, hold the resultant force $P = p_0\ell$ fixed and take the limit $\ell \to 0$. The finite footprint becomes a concentrated moving force in the distributional sense and its projected forcing approaches

$$\lim_{\ell\to 0} F_n(t) = \frac{2P}{L}(1+at)^r s(t)\sin(\kappa_n v t), \quad 0 < t < L/v. \tag{27}$$

For the no-foundation, non-induced, non-harmonic case ($k_f = N = a = 0$ and $s(t) = 1$), the well-known moving-point-force solution of each mode follows:

$$y_n(t) = \frac{2P}{\mu L}\frac{\sin(\kappa_n v t) - \left(\kappa_n v/\omega_n^{(0)}\right)\sin\left(\omega_n^{(0)} t\right)}{\left(\omega_n^{(0)}\right)^2 - (\kappa_n v)^2}, \qquad 0 \le t \le L/v. \tag{28}$$

At modal frequency matching $\kappa_n v = \omega_n^{(0)}$, the apparent zero denominator is removable and the corresponding finite-duration limit becomes

$$y_n^{(res)}(t) = \frac{P}{\mu L\left(\omega_n^{(0)}\right)^2}\left[\sin\left(\omega_n^{(0)} t\right) - \omega_n^{(0)} t\cos\left(\omega_n^{(0)} t\right)\right]. \tag{29}$$

As a separate check, a suddenly applied spatially sinusoidal stationary force $q(x,t) = q_s\sin(\kappa_1 x)H(t)$ produces only the first mode and yields $y_1(t) = (q_s/K_1)[1 - \cos(\omega_1 t)]$, where $K_1 = EI\kappa_1^4 + N\kappa_1^2 + k_f$. For fixed non-resonant forcing, the corresponding quasi-static deflection tends to zero as $k_f \to \infty$. The limit of an infinitely stiff foundation is an idealisation, not experimental validation or a replacement for supported beam conditions.

Third, with $k_f = N = a = 0$ but $s(t) = \sin(\Omega t)$, the moving-point-force forcing contains the two sidebands $|\Omega \pm \kappa_n v|$. The harmonic limit is thus recovered by substituting the sideband forcing into the same convolution. These are analytical **consistency tests**. Independent agreement with finite elements must be established through separate computed comparisons, not presumed from the closed-form reduction alone.

2.7. Numerical solution and finite-element verification

For each Fourier mode, a second evaluation is obtained from the average-acceleration Newmark time-stepping scheme ($\gamma = 1/2$, $\beta_N = 1/4$), using the same projected force history as in the convolution integral [29]. The solution is evaluated at sufficiently small time increments to resolve both the moving contact events and harmonic oscillations. We assess mode-count convergence separately for displacement, bending moment, and shear; the latter two depend on higher spatial derivatives and may require more modes than midspan deflection.

An independent finite-element formulation uses standard cubic Hermite Euler–Bernoulli beam elements with nodal displacement and slope degrees of freedom [30]. For element interpolation $w_e = \mathbf{N}_e\mathbf{d}_e$, the consistent mass and stiffness matrices are

$$\mathbf{M}_e = \int_{x_a}^{x_b} \mu\,\mathbf{N}_e^T\mathbf{N}_e\,dx, \tag{30}$$

$$\mathbf{K}_e = \int_{x_a}^{x_b}\left(EI\mathbf{N}_{e,xx}^T\mathbf{N}_{e,xx} + N\mathbf{N}_{e,x}^T\mathbf{N}_{e,x} + k_f\mathbf{N}_e^T\mathbf{N}_e\right)dx. \tag{31}$$

The element load vector is integrated only over the intersection of the element and current footprint:

$$\mathbf{f}_e(t) = p_0(1+at)^r s(t)\int_{[x_a,x_b]\cap[c(t),b(t)]}\mathbf{N}_e^T\,dx. \tag{32}$$

ISSN 2278-2540 | DOI: 10.51583/IJLTEMAS | Volume XV, Issue IX, September 2026

The global system $\mathbf{M}_{FE}\ddot{\mathbf{d}} + \mathbf{K}_{FE}\mathbf{d} = \mathbf{f}_{FE}(t)$ is assembled using independent shape functions and solved by Newmark integration. The end deflections are restrained while rotations remain free. Agreement is evaluated using peak deflection, time of peak, complete time histories, and the normalised root-mean-square error (NRMSE):

$$\mathrm{NRMSE}(\%) = \frac{100}{\max_i |w_i^{FE}|}\sqrt{\frac{1}{N_t}\sum_{i=1}^{N_t}\left(w_i^{FS} - w_i^{FE}\right)^2}. \tag{33}$$

Here FS and FE denote the independent Fourier-sine and finite-element response samples at the same observation point and time instants. Validation against field or laboratory measurements is **not** claimed in the absence of such data.

2.8.Response measures and dimensional consistency

The maximum absolute displacement at any observation point x_o is

$$w_{\max}(x_o) = \max_{0\le t\le T}|w(x_o,t)|. \tag{34}$$

For the classical Euler–Bernoulli convention adopted here, the bending moment and bending-shear resultant are

$$M(x,t) = -EIw_{xx}(x,t), \qquad V(x,t) = -EIw_{xxx}(x,t). \tag{35}$$

Peak harmonic-to-non-oscillatory response ratios are evaluated using the *same* beam, support, velocity, footprint, and reference intensity:

$$R_{HC} = \frac{\max_{0\le t\le T}|w_H(x_o,t)|}{\max_{0\le t\le T}|w_C(x_o,t)|}. \tag{36}$$

The dimensional requirements are $[EI] = \mathrm{N\,m^2}$, $[N] = \mathrm{N}$, $[\mu] = \mathrm{kg/m}$, $[k_f] = \mathrm{N/m^2}$, $[p_0] = \mathrm{N/m}$, $[a] = \mathrm{s^{-1}}$, and $[\Omega] = [\omega_n] = \mathrm{s^{-1}}$. Therefore, every term in the beam equilibrium equation has units of N/m. Where the older manuscript reports a foundation modulus in N/m³, the effective width used to obtain a line-foundation coefficient must be explicitly declared before those values are transferred to this formulation.

3. RESONANCE ANALYSIS

3.1. Natural frequencies and modal excitation frequencies

The natural circular frequencies of the simply supported, uniform Euler–Bernoulli beam–foundation system are

$$\omega_n = \sqrt{\frac{EI(n\pi/L)^4 + N(n\pi/L)^2 + k_f}{\mu}}, \qquad f_n = \frac{\omega_n}{2\pi}. \tag{37}$$

They are independent of the induced-load rate a because a modifies only the prescribed forcing. The frequency generated by translation of a load footprint across the n-th sine mode is $\lambda_n = \kappa_n v = n\pi v/L$. During the stage of complete footprint contact, the spatial projection includes the footprint-filter factor $\sin(\kappa_n \ell/2)$. Accordingly, a frequency match produces little or no excitation of a mode if this factor vanishes.

3.2. Nominal critical velocities for constant-intensity passage

For non-harmonic loading with $a = 0$, the modal forcing has carrier frequency λ_n. A nominal frequency-matching condition is

ISSN 2278-2540 | DOI: 10.51583/IJLTEMAS | Volume XV, Issue IX, September 2026

$$\lambda_n = \omega_n, \tag{38}$$

which gives the modal critical-speed estimate

$$v_{cr,n} = \frac{\omega_n}{\kappa_n} = \frac{L}{n\pi}\sqrt{\frac{EI(n\pi/L)^4 + N(n\pi/L)^2 + k_f}{\mu}}. \tag{39}$$

The nominal modal critical velocity defined by Equation (39) has dimensions of speed and is independent of the observation time. Since the distributed force acts over a finite contact region and for a limited passage duration, frequency matching does not imply unbounded steady-state resonance. The largest transient displacement may therefore occur at a travelling speed different from the nominal critical value, depending on the duration of contact, excitation phase, load-footprint averaging, and modal interaction.

3.3. Harmonic Excitation and Resonance Characteristics

The introduction of harmonic variation into the moving distributed load produces additional frequency components arising from the interaction between the imposed oscillatory excitation and the translational motion of the load. For the harmonic loading function $s(t) = \sin(\Omega t)$, the generalised force associated with the n-th mode contains frequency components governed by the imposed angular frequency Ω and the travelling-load frequency $\kappa_n v$, where $\kappa_n = n\pi/L$. When the load footprint is fully within the beam span, the product of these oscillatory contributions produces the sum and difference frequencies. Accordingly, the candidate resonance conditions are expressed as

$$\omega_n = |\Omega - \kappa_n v| \quad \text{or} \quad \omega_n = \Omega + \kappa_n v. \tag{40}$$

Here, ω_n denotes the natural angular frequency of the n-th vibration mode. The foregoing relations identify potential frequency interactions associated with dynamic amplification as the excitation frequencies approach the modal natural frequencies of the beam–foundation system. For prescribed values of Ω and ω_n, the corresponding non-negative candidate critical velocities are

$$v_{cr,n}^{(H,1)} = \frac{|\omega_n - \Omega|}{\kappa_n}, \qquad v_{cr,n}^{(H,2)} = \frac{\omega_n + \Omega}{\kappa_n}. \tag{41}$$

The two expressions represent distinct frequency-matching branches of the harmonically excited structural system. The occurrence of a frequency match does not necessarily correspond to the largest transient displacement because the moving force occupies a finite contact region and excites the beam for a limited period. The response is additionally influenced by the loading phase, spatial distribution, induced-load envelope, and participation of the vibration modes. In particular, the finite footprint modifies the generalized force through the spatial factor $\sin(\kappa_n \ell/2)$; when this factor vanishes, the corresponding mode is not excited by the fully contained uniform load footprint, even at a nominal frequency match.

To quantify the relative magnitude of the transient response, the dynamic amplification factor (DAF) is defined at an interior observation point x_o as

$$\mathrm{DAF} = \frac{\max_{0\le t\le T}|w_{\mathrm{dyn}}(x_o,t)|}{\max_{0\le t\le T}|w_{\mathrm{qs}}(x_o,t)|}. \tag{42}$$

In this expression, $w_{\mathrm{dyn}}(x_o,t)$ and $w_{\mathrm{qs}}(x_o,t)$ are the dynamic and quasi-static displacements, respectively, and T is the simulation duration. The quasi-static response is evaluated using the elastic equilibrium equation with the same instantaneous position and prescribed magnitude of the moving distributed force, but without structural inertia. For the selected interior observation location, the denominator is required to be nonzero. This definition therefore provides a consistent comparison of the transient and quasi-static displacement amplitudes under a common loading history.

The derived relations identify *candidate* resonance conditions for the idealized beam-foundation model. Because the moving excitation has finite duration, its frequency content is broadened by load entry and exit, and the magnitude of dynamic amplification depends on the complete forcing history rather than on frequency matching alone.

ISSN 2278-2540 | DOI: 10.51583/IJLTEMAS | Volume XV, Issue IX, September 2026

3.4. Influence and Physical Interpretation of the Induced-Load Factor

The time-dependent intensity of the prescribed distributed moving load is represented by the power-law envelope $p(t) = p_0(1 + at)^r$, where p_0 is the initial force intensity, a is the induced-load rate, and r is the dimensionless power-law exponent. The parameter a has units of s^{-1}, so the quantity $1 + at$ is dimensionless. The model is considered over a time interval satisfying $1 + at > 0$ for general real values of r.

For $r > 0$, positive values of a describe increasing load intensity during traversal, whereas negative values of a describe a decreasing intensity over the admissible interval. The limiting case $a = 0$ recovers a constant-amplitude distributed moving load. In the harmonic case, this envelope multiplies $\sin(\Omega t)$ and thus modulates a signed oscillatory force component. The induced-load factor represents prescribed temporal variation of the applied force; it does not constitute a moving-mass model or introduce additional inertia into the governing equation.

Changes in the induced-load rate modify the magnitude and temporal distribution of the external excitation and consequently affect the transient transverse displacement. Although increasing the force envelope may increase vibration amplitudes, the maximum response also depends on the travelling velocity, excitation frequency, load contact length, foundation stiffness, and modal phase relations. Accordingly, the response associated with the induced-load factor is determined from the parameter-dependent calculations rather than assumed to vary monotonically under all excitation conditions.

Because the power-law envelope modifies the external forcing rather than the beam stiffness or mass distribution, the induced-load parameter does not change the natural frequencies of the linear beam-foundation system. Its influence is instead manifested in the distribution of energy supplied to the vibration modes during load traversal. Under harmonic loading, the envelope modifies the amplitudes of the excitation components and their resulting transient responses without independently defining a new natural frequency of the structure.

The analytical results are based on linear Euler-Bernoulli beam theory, uniform Winkler foundation resistance, prescribed moving-force excitation, and simply supported boundary conditions. Transverse shear deformation, rotary inertia, structural damping, moving-mass inertia, nonlinear foundation response, and spatially varying structural properties are excluded from this formulation. Consequently, the predicted frequencies, critical-speed estimates, and amplification factors are interpreted as properties of the specified mathematical model rather than site-specific design limits for a railway track or bridge.

3.5 Nomenclature

The symbols employed in the governing equations, analytical solution, resonance analysis, and numerical computations are defined in Table 1. Unless otherwise specified, all quantities are expressed in SI units.

Symbol	Description	SI unit
x	Longitudinal coordinate	M
t, T	Time and simulation duration	S
L, ℓ	Beam span and load contact length	M
$w(x,t)$	Transverse displacement	M
$w_{\mathrm{dyn}}, w_{\mathrm{qs}}$	Dynamic and quasi-static transverse displacement	M
x_o	Observation position	M
E	Young's modulus	Pa
I	Second moment of cross-sectional area	m^4
EI	Flexural rigidity	$N{\cdot}m^2$
A	Beam cross-sectional area	m^2
ρ	Mass density	kg/m^3
$\mu = \rho A$	Mass per unit length	kg/m
N	Uniform tensile axial force	N

ISSN 2278-2540 | DOI: 10.51583/IJLTEMAS | Volume XV, Issue IX, September 2026

Symbol	Description	SI unit
k_f	Winkler foundation stiffness per unit beam length and displacement	N/m^2
$q(x,t)$	Applied distributed transverse loading	N/m
$p_0, p(t)$	Initial load intensity and time-dependent intensity envelope	N/m
$P(t)$	Resultant applied force over the active contact region	N
a, r	Induced-load rate and power-law exponent	s^{-1}; dimensionless
$v, v_{cr,n}$	Load velocity and nominal modal critical velocity	m/s
$H, \chi(x,t)$	Heaviside step function and footprint indicator	dimensionless
$c(t), b(t)$	Left and right endpoints of active load footprint	M
n, N_m	Mode number and number of retained modes	dimensionless
$\kappa_n = n\pi/L$	Modal wavenumber	m^{-1}
$\phi_n(x)$	Admissible sine mode shape	dimensionless
$y_n(t)$	Modal displacement coordinate	M
$F_n(t)$	Normalized generalized modal load intensity	N/m
ω_n, f_n	Natural angular and cyclic frequency	rad/s; Hz
Ω	Imposed harmonic angular frequency	rad/s
$\kappa_n v$	Travelling-load modal angular frequency	rad/s
$M(x,t), V(x,t)$	Bending moment and transverse shear resultant	N·m; N
Δt	Numerical integration time increment	S
γ, β_N	Newmark time-integration parameters	dimensionless
δ	Dirac delta distribution in the concentrated-force limit	m^{-1}
DAF	Dynamic amplification factor	dimensionless

4. NUMERICAL RESULTS AND DISCUSSION

The numerical study examines the behaviour of a simply supported uniform Euler–Bernoulli beam subjected to a finite-length distributed moving force whose intensity is constant, power-law modulated, or harmonically modulated. The analyses directly address the reviewers' requests for limiting-case verification, modal and time-step convergence, finite-element comparison, natural frequencies, resonance characteristics, parametric sensitivity, bending moments, and shear forces. All numerical values below were recalculated for the explicitly specified illustrative baseline; they are not experimental measurements and do not reproduce the original manuscript's incompletely specified graphs.

4.1. Baseline problem and comparative design

A 50.192 m beam of rectangular section 0.40 m × 0.80 m was modelled with E = 210 GPa, ρ = 7850 kg/m³, EI = 3.584 × 10⁹ N·m², and μ = 2512 kg/m. Unless otherwise stated, the Winkler line-stiffness coefficient was k_f = 0.20 MN/m², the uniform tensile prestress was N = 0, the reference moving-load intensity was p_0 = 9 kN/m, the contact length was ℓ = 3 m, and the speed was v = 12.5 m/s. A linear induced envelope, $p(t) = p_0(1 + at)$, was adopted (power exponent r = 1). The fundamental comparisons used a = 0, 32 Fourier modes, 100 two-node cubic Hermite finite elements, and Δt = 0.005 s. The load completely exited the beam at 4.255 s, and responses were continued for approximately 1.3 s to capture free vibration.

4.2. Natural frequencies and admissible mode shapes

The natural frequencies were obtained from $\omega_n^2 = [EI(n\pi/L)^4 + N(n\pi/L)^2 + k_f]/\mu$, with $f_n = \omega_n/(2\pi)$. Figure 2 shows the first three simply supported mode shapes. These satisfy the end-displacement and zero-end-moment conditions and define the spatial basis used in the Fourier solution. The nominal speed $\mathbf{v_{cr,n}} = \omega_n L/(n\pi)$ describes a mode-dependent frequency-matching condition; it does not guarantee the largest finite-passage response.

ISSN 2278-2540 | DOI: 10.51583/IJLTEMAS | Volume XV, Issue IX, September 2026

Table 2. Calculated natural frequencies and nominal matching speeds (baseline).

Mode	Frequency, f_n (Hz)	ω_n (rad/s)	$v_{cr,n}$ (m/s)
1	1.6036	10.0755	160.973
2	3.3003	20.7362	165.647
3	6.8518	43.0509	229.269
4	12.0007	75.4028	301.17
5	18.6735	117.329	374.903

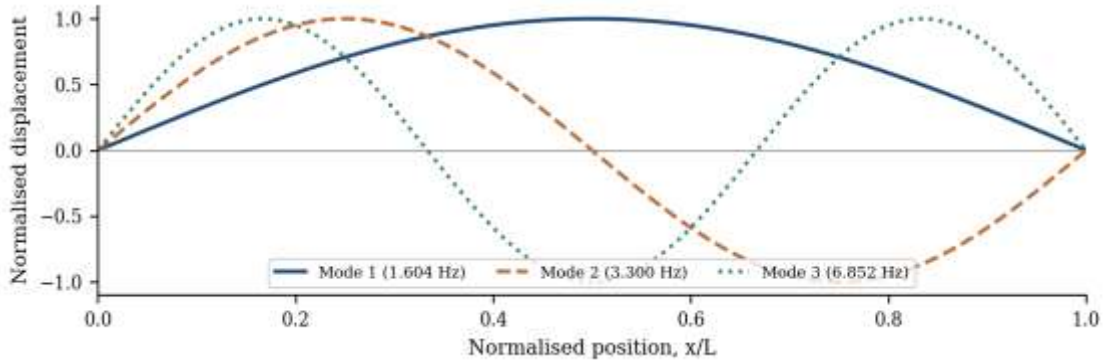


Figure 2. First three normalized mode shapes of the simply supported beam; natural frequencies are indicated in the legend.

4.3. Modal convergence, time-step sensitivity and mesh refinement

The Fourier series was tested against a 64-mode reference. Peak midspan displacement converged rapidly, with the 12-mode peak differing by approximately 0.0203% and the 32-mode peak by less than 0.0001% relative to the 64-mode calculation. Time-history NRMSE for 12 modes was 0.0081%. At exact midspan, even sine modes make no direct contribution, but they remain necessary for evaluating displacement away from the centre and spatial derivatives. The number of retained modes is especially important for bending moment and shear because these involve second and third spatial derivatives.

Table 3. Fourier-series convergence relative to the 64-mode reference.

Modes	Peak (mm)	Peak difference (%)	Time-history NRMSE (%)
1	4.39279	−4.4294	3.0183
3	4.58089	−0.3369	0.4067
8	4.59849	+0.0459	0.0383
12	4.59731	+0.0203	0.0081
16	4.59660	+0.0049	0.0023
24	4.59636	−0.0004	0.0002
32	4.59638	−0.0001	0.00004
64	4.59638	0	0

ISSN 2278-2540 | DOI: 10.51583/IJLTEMAS | Volume XV, Issue IX, September 2026

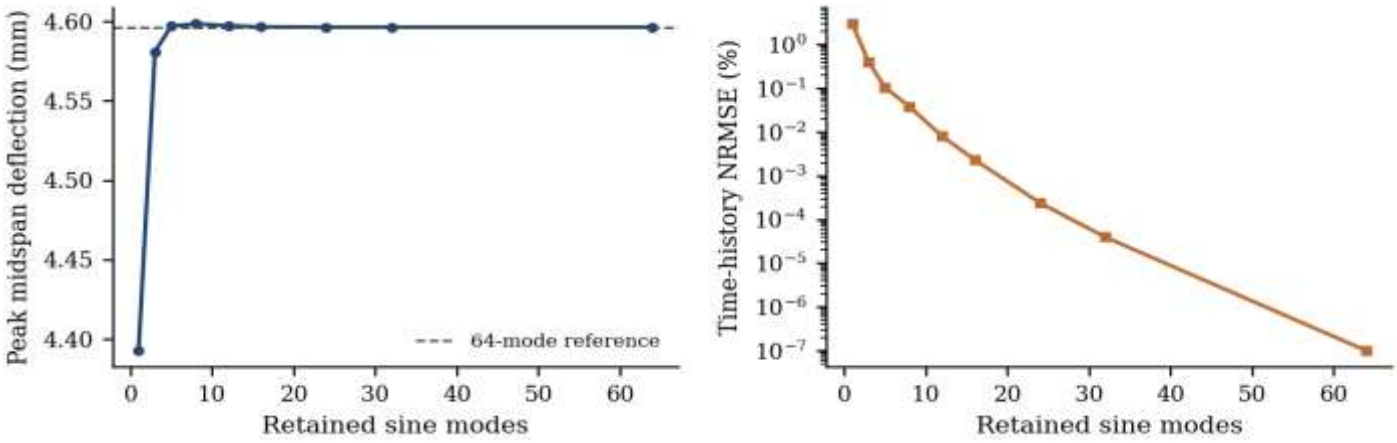


Figure 3. Convergence of maximum midspan displacement and complete displacement history as the number of retained Fourier modes increases.

Time-step refinement produced peaks of 4.60028, 4.59903, 4.59638, 4.59561, and 4.59547 mm for Δt = 0.020, 0.010, 0.005, 0.0025, and 0.00125 s, respectively. Thus, the standard 0.005 s result differs from the finest tested step by approximately 0.020%. Independent finite-element refinement from 20 to 160 elements changed the peak by less than 0.00001 mm. These tests support the reported displacement accuracy for the selected loading, but are not a substitute for higher-resolution checks of shear near moving footprint boundaries.

4.4. Limiting-case validation and independent finite-element comparison

Three consistency tests were used: removing the foundation ($k_f = 0$), strengthening the elastic support, and shrinking the footprint while maintaining the total resultant. For the unfounded first-mode moving-point-force limit, the analytical displacement at t = 2.0075 s was 20.01789 mm. Replacing the point load with a 0.01 m footprint produced 20.01158 mm (0.0315% difference); a 0.001 m footprint reduced the difference to approximately 0.0032%. This establishes convergence to the classical moving-point-force projection without equating a finite footprint to a point load.

The second verification method used independently assembled cubic Hermite Euler–Bernoulli elements with consistent mass, foundation stiffness, and moving-force integration, integrated using the same average-acceleration Newmark scheme. The agreement in Table 4 is exceptionally close for the selected cases, verifying the independent spatial discretisation and their force projection. Because both methods solve the same idealised model, the comparison establishes numerical verification rather than experimental validation.

Table 4. Fourier–finite-element verification of peak midspan displacement.

Case	Fourier (mm)	FE (mm)	Peak difference (%)	NRMSE (%)
Unfounded, constant	22.865786	22.865789	0.000015	0.000008
Supported, constant	4.596377	4.596379	0.000057	0.000040
Supported, harmonic $0.5\omega_1$	6.536897	6.536903	0.000093	0.000022
Supported, harmonic ω_1	54.290035	54.290035	<0.000001	0.000002

ISSN 2278-2540 | DOI: 10.51583/IJLTEMAS | Volume XV, Issue IX, September 2026

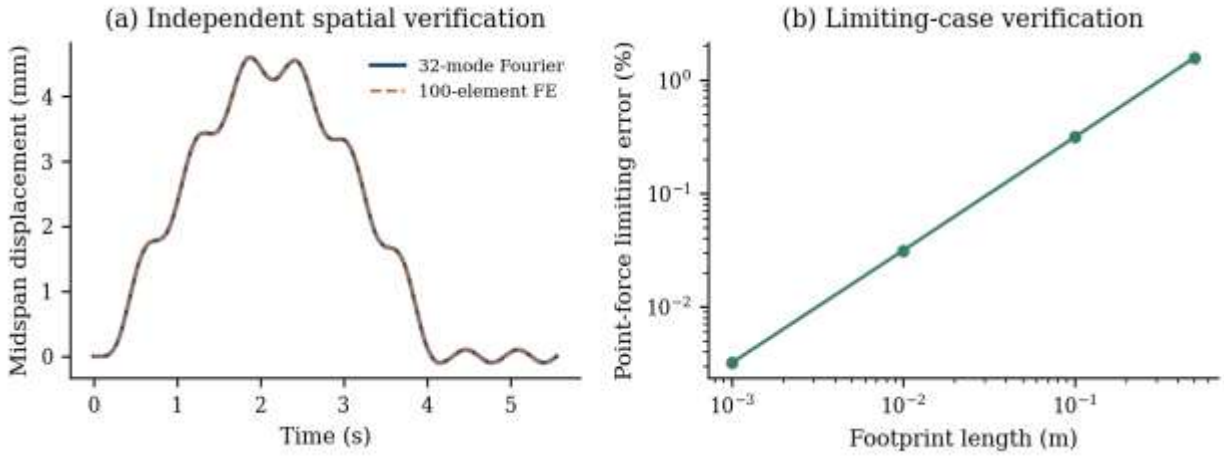


Figure 4. (a) Superposed Fourier and independently assembled finite-element time histories. (b) Reduction in the error against the analytical moving-point-force limit as the footprint length approaches zero.

4.5. Influence of Winkler foundation stiffness

The influence of the Winkler foundation was assessed while fixing the beam geometry, load intensity, footprint, and speed. Increasing the line-stiffness coefficient reduced the maximum transverse displacement in the investigated range, from 22.86579 mm without the foundation to 4.59638 mm at the reference coefficient of 0.20 MN/m², equivalent to a 79.90% reduction. The peak decreased further to 1.26272 mm at 1.0 MN/m² and 0.12744 mm at 20 MN/m². The latter result illustrates increasing foundation restraint and a tendency toward vanishing displacement as stiffness increases; it does not define a separate rigid-foundation closed-form solution.

Table 5. Foundation-stiffness sensitivity under non-oscillatory moving loading (a = 0).

k_f (MN/m²)	Peak midspan deflection (mm)	Change relative to $k_f = 0$ (%)
0.00	22.86579	0
0.05	11.46317	−49.86
0.10	7.77526	−65.99
0.20	4.59638	−79.90
0.60	1.90475	−91.67
1.00	1.26272	−94.48
20.00	0.12744	−99.44

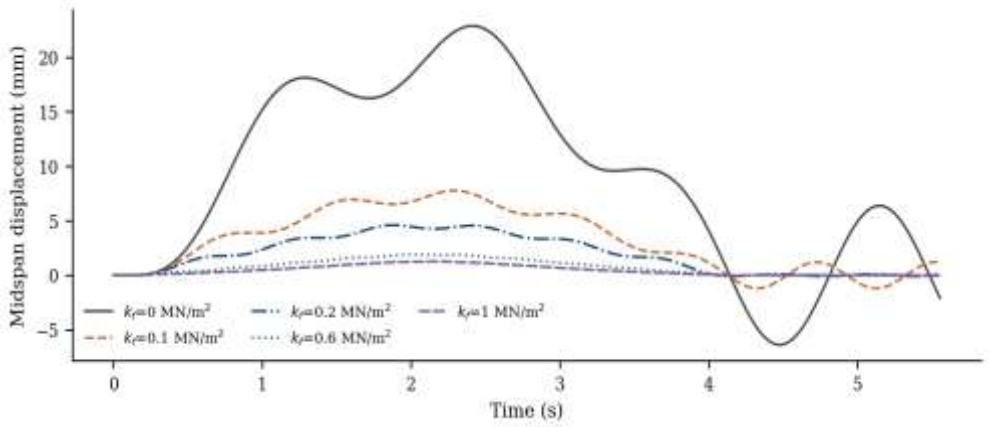


Figure 5. Midspan deflection histories for selected Winkler line-stiffness coefficients (p_0 = 9 kN/m, ℓ = 3 m, v = 12.5 m/s, a = 0, N = 0).

ISSN 2278-2540 | DOI: 10.51583/IJLTEMAS | Volume XV, Issue IX, September 2026

4.6. Effect of the induced-load factor

For r = 1, the induced-rate coefficient a (s^{-1}) governs the prescribed load envelope $p(t) = p_0(1 + at)$. In the positive-rate range investigated, raising a from 0 to 0.20 s^{-1} increased the peak displacement from 4.59638 to 6.64399 mm, a rise of 44.55%. The corresponding maximum absolute midspan bending moment increased from 109.69 to 157.80 kN·m, while the modal quarter-span bending-shear indicator increased from 11.87 to 14.91 kN. These results correct the contradictory statements about the induced factor in the original paper. The increase is demonstrated for the specified positive linear envelope and parameter range, not asserted universally for arbitrary time-dependent loads.

Table 6. Induced-rate effects under the constant-envelope moving-force model.

a (s^{-1})	Peak w(L/2) (mm)	Peak |M(L/2)| (kN·m)	Peak |V(L/4)| (kN)
0.00	4.5964	109.69	11.87
0.05	5.0750	121.70	12.63
0.10	5.5977	133.72	13.38
0.20	6.6440	157.80	14.91

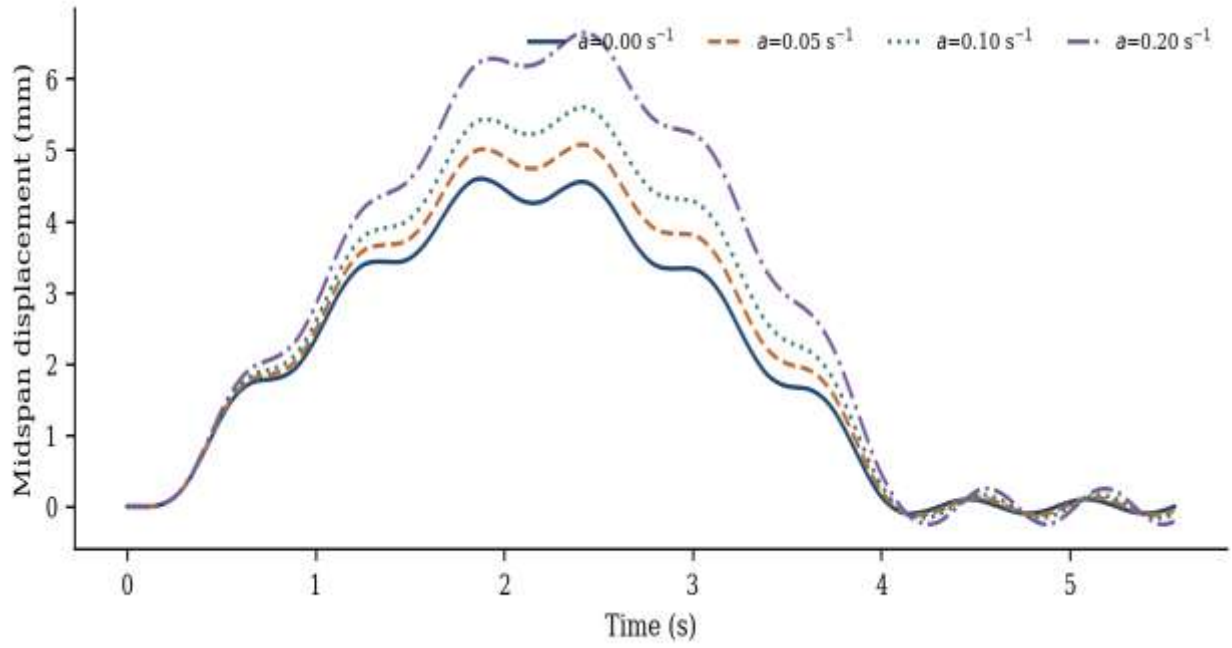


Figure 6. Comparison of midspan displacement histories for positive induced-load rates, with identical beam, foundation, and travelling-load parameters.

4.7. Constant and harmonic excitations, frequency content and resonance

The non-oscillatory force and the signed harmonic excitation were compared using identical values of L, EI, μ, k_f, ℓ, v, p_0, and a = 0. The non-oscillatory case gave a 4.59638 mm peak; the harmonic cases yielded 6.53690 mm at $\Omega/\omega_1 = 0.5$, 36.54004 mm at 0.9, and 54.29004 mm at 1.0. At the selected frequency $\Omega = \omega_1$, the peak ratio of harmonic to non-oscillatory response was 11.81. This large undamped transient response developed during and after passage but depends strongly on excitation frequency: at $\Omega/\omega_1 = 1.5$ the peak fell to 3.74992 mm. Consequently, harmonic loads cannot generally be assumed to produce greater vibration than constant loads.

ISSN 2278-2540 | DOI: 10.51583/IJLTEMAS | Volume XV, Issue IX, September 2026

A travelling harmonic load excites nominal sidebands $|\Omega \pm n\pi v/L|$. These frequencies may approach the modal natural frequencies, but the location of a finite-passage response maximum is affected by footprint filtering, traversal time, and phase. The frequency sweep therefore provides a stronger basis for identifying near-resonant amplification than a single frequency-matching statement.

Table 7. Harmonic-frequency sensitivity at the baseline parameters.

Excitation case	Ω/ω_1	Peak deflection (mm)	Peak ratio to constant load
Non-oscillatory	—	4.59638	1.00
Harmonic	0.50	6.53690	1.42
Harmonic	0.90	36.54004	7.95
Harmonic	1.00	54.29004	11.81
Harmonic	1.25	10.80314	2.35
Harmonic	1.50	3.74992	0.82

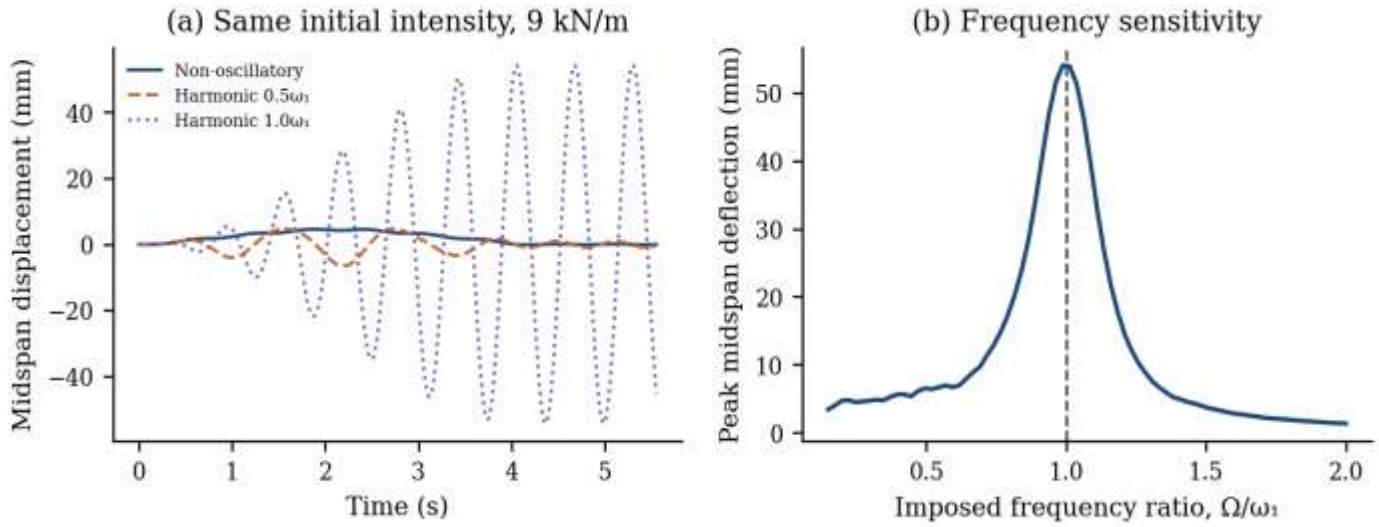


Figure 7. (a) Comparison of non-oscillatory and harmonically modulated moving loads with identical reference intensity; (b) sensitivity of the transient peak to Ω/ω_1.

The windowed response spectrum in Figure 8 is dominated by energy near the first natural frequency in the selected harmonic case, consistent with the large transient response. The finite observation interval limits frequency resolution, and the computed periodogram is not a measured vibration spectrum. In addition, the harmonic force $p_0 \sin(\Omega t)$ changes sign; it represents a dynamic excitation component rather than the complete non-negative contact force of a moving vehicle.

ISSN 2278-2540 | DOI: 10.51583/IJLTEMAS | Volume XV, Issue IX, September 2026

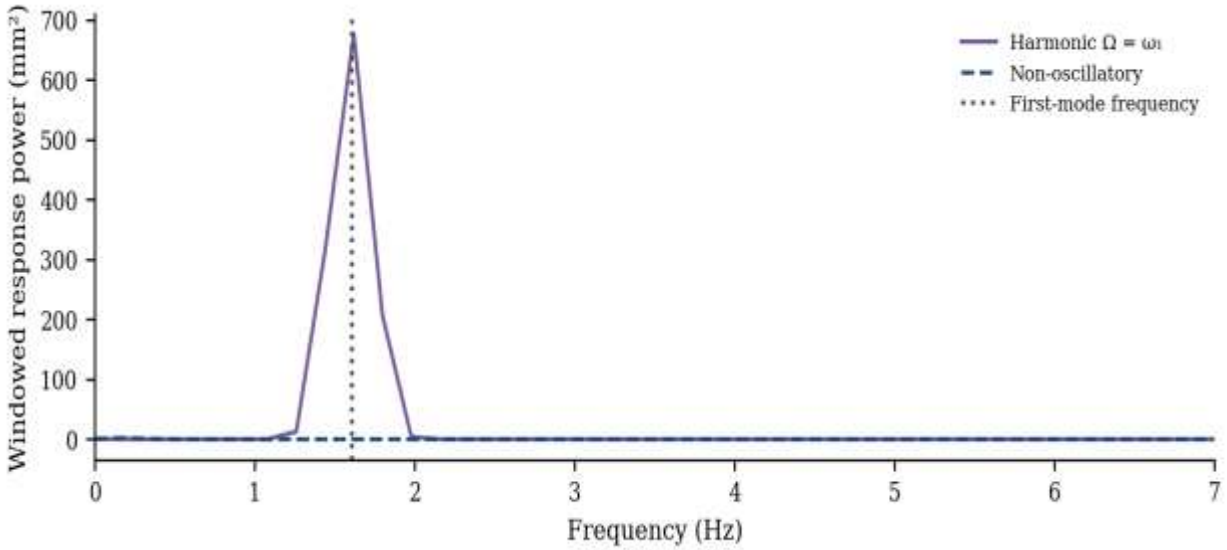


Figure 8. Windowed frequency spectrum of computed midspan displacement for the non-oscillatory and first-frequency harmonic cases; the vertical reference marks f_1 = 1.604 Hz.

4.8. Travelling velocity and beam-length sensitivity

Peak response varies non-monotonically with moving speed. Within the sampled velocities, the largest calculated constant-load response was 7.4173 mm at v = 125 m/s, whereas the first nominal frequency-matching speed was 160.973 m/s. At 160.973 m/s, the computed peak was 7.1579 mm. This difference arises from the finite footprint, limited force residence time, and modal phase and illustrates why a nominal critical speed is not necessarily the speed of maximum transient displacement. Increasing speed eventually shortened the traversal sufficiently to reduce the peak; at 250 m/s the peak was 5.8874 mm.

Changing beam length while retaining cross-sectional and material properties, load intensity, contact length, speed, and line-foundation coefficient also produced a non-monotonic trend. Peaks were 4.3871, 4.6164, 4.5964, 4.6442, 4.6363, and 4.3539 mm for spans of 40, 45, 50.192, 55, 60, and 70 m, respectively. These are parameter sensitivities of the chosen model, not prescriptions for allowable bridge spans or vehicle speeds.

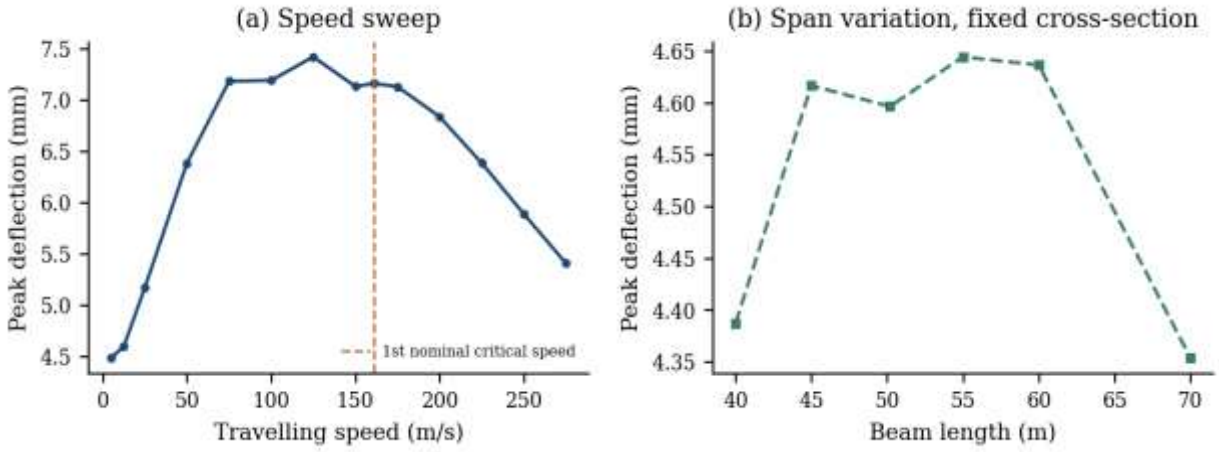


Figure 9. (a) Speed-dependent maximum midspan displacement and the first nominal matching speed; (b) beam-length sweep with unchanged cross-section and reference load parameters.

4.9. Bending moment and bending shear

For the Euler-Bernoulli baseline with N = 0, bending moment and bending shear were reconstructed from $M(x,t) = -EI\, w_{xx}$ and $V(x,t) = -EI\, w_{xxx}$, respectively, with signs depending on the chosen sectional convention.

ISSN 2278-2540 | DOI: 10.51583/IJLTEMAS | Volume XV, Issue IX, September 2026

The induced-load envelope increased the magnitudes of both internal actions, as quantified in Table 6. Unlike transverse displacement, shear involves the third spatial derivative of the modal series, and convergence near abrupt load-footprint boundaries is more demanding. The quarter-span shear reported here is therefore explicitly labelled a modal bending-shear indicator and should not be treated as a directly measured support reaction.

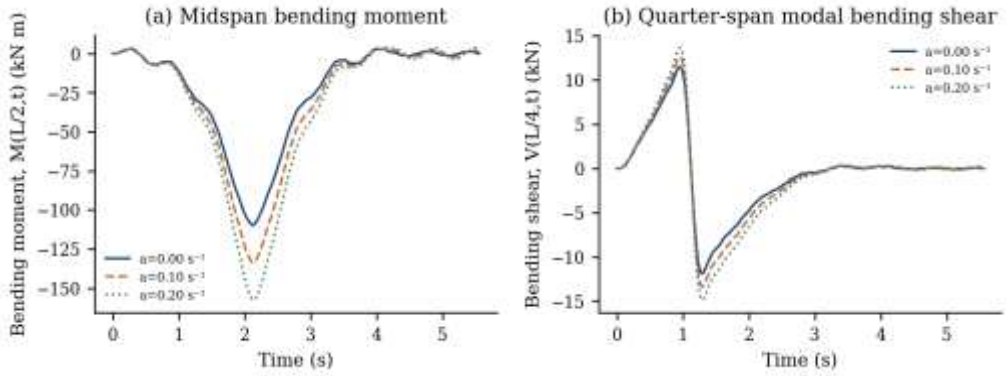


Figure 10. (a) Midspan bending moment and (b) quarter-span modal bending-shear histories for different induced-load rates (p_o = 9 kN/m, k_f = 0.20 MN/m², v = 12.5 m/s).

4.10. Engineering interpretation, limitations, and implications

The numerical results indicate that elastic restraint suppresses transverse deflection for the examined moving-force cases, whereas positive power-law load modulation can increase displacement and internal-force demands. Near the first modal frequency, signed harmonic excitation can produce large undamped transient amplitudes; the severity depends on the imposed frequency and load travel characteristics, and not merely on force magnitude. These trends are relevant when developing simplified vibration-screening models for beam-like transportation or industrial structures, but cannot be used as site-specific design predictions without calibration.

The analysis assumes a homogeneous, prismatic, linear Euler-Bernoulli beam, simply supported ends, a uniform linear Winkler foundation, prescribed moving-force loading, and no beam or foundation damping. It excludes moving-mass inertia, suspension and contact dynamics, shear deformation, rotary inertia, nonlinear support response, foundation heterogeneity, and geometric imperfections. Each omitted mechanism can alter natural frequencies, resonant amplification or internal forces. Independent Fourier-finite-element agreement establishes consistency of the numerical formulations; it does not establish field validation. The illustrative baseline and the revised finite-footprint force law also differ from the original submission and require author approval before journal submission.

3. CONCLUSIONS

This study investigated the dynamic response of a simply supported Euler–Bernoulli beam resting on a Winkler elastic foundation and subjected to constant and harmonically varying distributed moving loads incorporating a power-law induced-load factor. The governing fourth-order partial differential equation was solved using the Fourier sine-series method and convolution techniques, while the numerical solutions were independently verified using the finite-element method.

The results demonstrated that increasing foundation stiffness reduced transverse displacement, whereas increasing the positive induced-load rate amplified the vibration response under the investigated loading conditions. Harmonic excitation near the fundamental natural frequency produced considerably greater displacement than the corresponding constant-load case. For the selected parameters, foundation stiffness reduced the peak displacement by approximately 79.90%, while increasing the induced-load rate from 0 to 0.20 s^{-1} increased the peak response by 44.55%. The numerical solutions exhibited close agreement with the finite-element predictions, confirming the computational consistency of the proposed formulation.

ISSN 2278-2540 | DOI: 10.51583/IJLTEMAS | Volume XV, Issue IX, September 2026

The study further established that dynamic amplification depends on travelling velocity, excitation frequency, load-contact duration, and foundation properties. These findings provide useful insight into the vibration characteristics of idealised beam–foundation systems under time-dependent moving loads. However, the formulation is restricted to linear, uniform Euler–Bernoulli beams with simply supported boundary conditions and prescribed moving-force excitation. Future investigations may incorporate structural damping, shear deformation, rotary inertia, nonlinear foundations, and moving-mass interactions to extend its engineering applicability.

REFERENCES

1. Frýba, L. (1999). *Vibration of solids and structures under moving loads* (3rd ed.). Thomas Telford. https://doi.org/10.1680/vosasuml.35393
2. Ouyang, H. (2011). Moving-load dynamic problems: A tutorial (with a brief overview). *Mechanical Systems and Signal Processing*, *25*(6), 2039–2060. https://doi.org/10.1016/j.ymssp.2010.12.010
3. Kenney, J. T. (1954). Steady-state vibrations of beam on elastic foundation for moving load. *Journal of Applied Mechanics*, *21*, 359–364. https://doi.org/10.1115/1.4010934
4. Museros, P., Moliner, E., & Martínez-Rodrigo, M. D. (2013). Free vibrations of simply-supported beam bridges under moving loads: Maximum resonance, cancellation and resonant vertical acceleration. *Journal of Sound and Vibration*, *332*(2), 326–345. https://doi.org/10.1016/j.jsv.2012.08.008
5. Yang, Y. B., Yau, J. D., & Hsu, L. C. (1997). Vibration of simple beams due to trains moving at high speeds. *Engineering Structures*, *19*(11), 936–944. https://doi.org/10.1016/S0141-0296(97)00001-1
6. Zhai, W., Han, Z., Chen, Z., Ling, L., & Zhu, S. (2019). Train–track–bridge dynamic interaction: A state-of-the-art review. *Vehicle System Dynamics*, *57*(7), 984–1027. https://doi.org/10.1080/00423114.2019.1605085
7. Lamprea-Pineda, A. C., Connolly, D. P., & Hussein, M. F. M. (2022). Beams on elastic foundations—A review of railway applications and solutions. *Transportation Geotechnics*, *33*, 100696. https://doi.org/10.1016/j.trgeo.2021.100696
8. Sayeed, M. A., & Shahin, M. A. (2023). Dynamic response analysis of ballasted railway track–ground system under train moving loads using 3D finite element numerical modelling. *Transportation Infrastructure Geotechnology*, *10*, 639–659. https://doi.org/10.1007/s40515-022-00238-2
9. Hetényi, M. (1946). *Beams on elastic foundation: Theory with applications in the fields of civil and mechanical engineering*. University of Michigan Press.
10. Saito, H., & Terasawa, T. (1980). Steady-state vibrations of a beam on a Pasternak foundation for moving loads. *Journal of Applied Mechanics*, *47*(4), 879–883. https://doi.org/10.1115/1.3153807
11. Dimitrovová, Z. (2010). A general procedure for the dynamic analysis of finite and infinite beams on piece-wise homogeneous foundation under moving loads. *Journal of Sound and Vibration*, *329*(13), 2635–2653. https://doi.org/10.1016/j.jsv.2010.01.017
12. Castro Jorge, P., Simões, F. M. F., & Pinto da Costa, A. (2015). Dynamics of beams on non-uniform nonlinear foundations subjected to moving loads. *Computers & Structures*, *148*, 26–34. https://doi.org/10.1016/j.compstruc.2014.11.002
13. Abu-Hilal, M., & Zibdeh, H. S. (2000). Vibration analysis of beams with general boundary conditions traversed by a moving force. *Journal of Sound and Vibration*, *229*(2), 377–388. https://doi.org/10.1006/jsvi.1999.2491
14. Abu-Hilal, M., & Mohsen, M. (2000). Vibration of beams with general boundary conditions due to a moving harmonic load. *Journal of Sound and Vibration*, *232*(4), 703–717. https://doi.org/10.1006/jsvi.1999.2771
15. Esmailzadeh, E., & Ghorashi, M. (1995). Vibration analysis of beams traversed by uniform partially distributed moving masses. *Journal of Sound and Vibration*, *184*(1), 9–17. https://doi.org/10.1006/jsvi.1995.0301
16. Wu, Y., & Gao, Y. (2015). Analytical solutions for simply supported viscously damped double-beam system under moving harmonic loads. *Journal of Engineering Mechanics*, *141*(7), 04015004. https://doi.org/10.1061/(ASCE)EM.1943-7889.0000900
17. Şimşek, M., & Kocatürk, T. (2009). Free and forced vibration of a functionally graded beam subjected to a concentrated moving harmonic load. *Composite Structures*, *90*(4), 465–473.

ISSN 2278-2540 | DOI: 10.51583/IJLTEMAS | Volume XV, Issue IX, September 2026

https://doi.org/10.1016/j.compstruct.2009.04.024

18. Şimşek, M., & Al-Shujairi, M. (2017). Static, free and forced vibration of functionally graded (FG) sandwich beams excited by two successive moving harmonic loads. *Composites Part B: Engineering*, *108*, 18–34. https://doi.org/10.1016/j.compositesb.2016.09.098
19. Calim, F. F. (2016). Free and forced vibration analysis of axially functionally graded Timoshenko beams on two-parameter viscoelastic foundation. *Composites Part B: Engineering*, *103*, 98–112. https://doi.org/10.1016/j.compositesb.2016.08.008
20. Li, Z., Xu, Y., & Huang, D. (2021). Analytical solution for vibration of functionally graded beams with variable cross-sections resting on Pasternak elastic foundations. *International Journal of Mechanical Sciences*, *191*, 106084. https://doi.org/10.1016/j.ijmecsci.2020.106084
21. Su, J., Zhang, K., Zhang, Q., & Tian, Y. (2020). Free and forced vibration of coupled beam systems resting on variable viscoelastic foundations. *International Journal of Structural Stability and Dynamics*, *20*(12), 2050141. https://doi.org/10.1142/S0219455420501412
22. Ermis, M., Kutlu, A., Eratlı, N., & Omurtag, M. H. (2022). Free vibration of axially FG curved beam on orthotropic Pasternak foundation via mixed FEM. *Journal of the Brazilian Society of Mechanical Sciences and Engineering*, *44*(12), 597. https://doi.org/10.1007/s40430-022-03853-9
23. Vu, A. N. T., Le, N. A. T., & Nguyen, D. K. (2021). Dynamic behaviour of bidirectional functionally graded sandwich beams under a moving mass with partial foundation supporting effect. *Acta Mechanica*, *232*, 2853–2875. https://doi.org/10.1007/s00707-021-02948-z
24. Adedowole, A. (2020). Transverse motions of Bernoulli-Euler beam resting on elastic foundation and under two concentrated moving loads. *Journal of Advances in Mathematics and Computer Science*, *34*(6), 1–21. https://doi.org/10.9734/JAMCS/2019/v34i630228
25. Omolofe, B., & Adedowole, A. (2019). Transverse response of a structural member with time dependent boundary conditions to moving distributed mass. *Journal of Applied Nonlinear Dynamics*, *8*(2), 167–187. https://doi.org/10.5890/JAND.2019.06.002
26. Omolofe, B., & Adara, E. O. (2020). Response characteristics of a beam-mass system with general boundary conditions under compressive axial force and accelerating masses. *Engineering Reports*, *2*(2), e12118. https://doi.org/10.1002/eng2.12118
27. Huang, Y., Liu, H., & Zhao, Y. (2023). Dynamic analysis of non-uniform functionally graded beams on inhomogeneous foundations subjected to moving distributed loads. *Applied Sciences*, *13*(18), 10309. https://doi.org/10.3390/app131810309
28. Chen, W. R., & Lin, C. H. (2024). Dynamic response of bidirectional functionally graded beams with elastic supports and foundations under moving harmonic loads. *Acta Mechanica*, *235*, 4833–4862. https://doi.org/10.1007/s00707-024-03975-2
29. Newmark, N. M. (1959). A method of computation for structural dynamics. *Journal of the Engineering Mechanics Division*, *85*(3), 67–94. https://doi.org/10.1061/JMCEA3.0000098
30. Bathe, K. J. (1996). *Finite element procedures*. Prentice Hall.